Contents list available at CBIORE journal website

International Journal of Renewable Energy Development

Journal homepage: https://ijred.cbiore.id

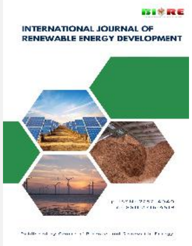

Research Article

Modelling and analysis of wind loading effects for heliostat mirrors using computational fluid dynamics

Naseer Ahmad[a*], Hafiz Muhammad Waqas Badar[a,b], Khurram Hameed Mughal[a,c], Hafiz Umar Ali[a], Muhammad Waqas[a,d]

[a] *Department of Mechanical Engineering, University of Engineering and Technology (Main Campus), Lahore, Pakistan*

[b] *CMT-Motores Termicos, Universidad Politecnica de Valencia, Camino de Vera s/n. 46022 Valencia, Spain*

[c] *Mechanical Engineering Department, Faculty of Engineering & Technology, The University of Lahore, Lahore 54800, Pakistan*

[d] *Faculty of Mechanical Engineering and Design, Kaunas University of Technology, Kaunas, Lithuania*

Abstract. This study examines the impact of wind forces on the structural integrity of heliostat assemblies in concentrated solar power systems, specifically tailored to local climatic conditions. The objective is to assess how varying elevation angles influence aerodynamic parameters, thereby informing design optimizations for enhanced operational efficiency. A computational fluid dynamics approach, utilizing the standard k-ε turbulence model, second-order implicit time formulation, and the Green-Gauss cell-based method, was employed to simulate wind interactions with a heliostat model at elevation angles of 0°, 30°, 60°, and 90°. The simulation process encompassed model development, mesh refinement, boundary condition setup, and numerical solution techniques. Post-processing analysis focused on aerodynamic characteristics such as drag and lift forces, static and dynamic pressures, turbulent kinetic energy, and turbulence intensity. Results indicate that drag force increases with elevation angle, peaking at 90°, while lift force is maximized at 30°. Additionally, static and dynamic pressures, skin friction coefficients, and turbulence parameters exhibit strong dependence on the heliostat's elevation angle. The minimum values of the skin friction coefficient, drag coefficient, and turbulence intensity were found to be 0.0111, 0.3580, and 11.42%, respectively, at an elevation angle of 0°. Moreover, the finite element analysis of the heliostat structure to evaluate its resistance under wind loading demonstrated structural integrity with acceptable stress and displacement levels. These findings provide valuable insights for engineers and researchers aiming to optimize heliostat structural dimensions, thereby enhancing the economic and operational performance of concentrated solar power systems.

Keywords: Computational fluid dynamics (CFD); Heliostat mirror, static pressure; turbulent kinetic energy; skin friction; wind loading effects

Received: 15th Dec 2024; Revised: 19th July 2025; Accepted: 30th August 2025; Available online: 12th Sept 2025

1. Introduction

The rising costs of fossil fuels, particularly oil, have significantly driven the transition to renewable energy sources in recent years. From 2000 to 2003, oil prices remained stable at around US$25 per barrel (Brent), with global demand increasing by just 1% annually (Kjärstad & Johnsson, 2009). However, as global energy demand continues to grow, particularly with economic development in emerging nations, there is a greater need for sustainable and economically viable energy alternatives (Kandpal & Broman, 2014). Global electricity generation is expected to double by 2035, presenting both challenges and opportunities for the energy sector (Dorian et al., 2006). Among the promising renewable technologies being developed to meet this demand are photovoltaics (PV), wind power, and concentrated solar power (CSP), each offering unique advantages for large-scale power production (Fuqiang *et al.*, 2017).

Concentrated solar power (CSP) is one of the most effective solutions for large-scale solar energy production, offering a viable alternative to traditional fossil-fuel-based electricity generation. CSP technology captures the sun's heat by focusing sunlight onto a receiver using mirrors. The collected energy is used to heat fluids, which produce steam that drives turbines to generate electricity. CSP systems typically fall into four categories: parabolic troughs, solar power towers, solar dish systems, and Fresnel reflectors (Devabhaktuni *et al.*, 2013; Sun *et al.*, 2014). Among these, solar power towers are particularly notable for their ability to generate significant power by concentrating solar energy onto a central receiver (Hinkley *et al.*, 2013; Abunajeeb *et al.*, 2025). CSP technology is an appealing renewable energy option due to its capacity for large-scale electricity production and its potential for thermal energy storage, allowing electricity generation even when the sun is not shining (Pavlovi *et al.*, 2012).

A key component of CSP systems is the heliostat-a large, motorized mirror that tracks the sun and directs sunlight toward

---

[*] Corresponding author
Email: nahmad@uet.edu.pk (N. Ahmad)

https://doi.org/10.61435/ijred.2025.60977

ISSN: 2252-4940/© 2025.The Author(s). Published by CBIORE

a receiver (TR *et al*., 2025). Heliostats are essential for achieving the high efficiencies required in CSP systems, and their performance and cost significantly influence the overall levelized cost of electricity (LCOE) for CSP plants. It is estimated that heliostats account for nearly 50% of the total cost of solar power tower projects (Emes *et al*., 2015). Therefore, reducing heliostat costs is critical to making CSP energy production more competitive with traditional energy sources. One effective approach for lowering these costs is optimizing the design and manufacturing of heliostats, particularly by improving the mechanical structures of the heliostat assemblies. To achieve this, understanding the various forces acting on heliostats-such as wind, gravity, and other environmental factors-is crucial for ensuring reliable performance and minimizing the risk of damage.

Wind forces are one of the most significant external loads that heliostats must withstand, impacting both their structural integrity and optical performance (Blume *et al*., 2023). Wind loads are typically categorized into dynamic loads, caused by turbulent winds, and static loads, associated with steady wind conditions (Coventry & Pye, 2014). Predicting these wind loads is crucial for designing heliostats capable of performing effectively under various wind conditions, as failure to account for them can lead to mechanical failure or costly downtime for maintenance. Emes *et al*. (2021) reviewed static and dynamic wind loads on heliostats, stressing the importance of accurately measuring turbulence to prevent structural damage and reduce costs. Their review focused on the aerodynamic effects of heliostat geometry, turbulence parameters, and field spacing. They recommended enhanced field-scale wind measurements to better characterize atmospheric boundary layer (ABL) turbulence, which could improve the accuracy of wind load predictions and reduce the capital cost of structural components in power tower plants. Grigoriev *et al*. (2022) analyzed heliostat field efficiency based on mirror density, showing that blocking and shadowing losses could be estimated without complex ray tracing or polygon clipping. By solving a variational problem, they identified an optimal mirror density distribution that maintains overall field efficiency. Emes *et al*. (2024) emphasized the significant role of wind loads in heliostat costs and the need for standardized methods to better understand static and dynamic wind loads in heliostat design. They identified gaps in site characterization, critical load cases, and the understanding of turbulence impact on heliostat tracking errors, recommending the development of guidelines for wind load and site characterization, along with models that account for wind loads and their effects on performance.

Several studies have explored the impact of wind on heliostat performance, focusing on how wind loads affect both the mechanical and optical aspects. Zang *et al*. (2014) analyzed wind flow around heliostats with varying aspect ratios in a high-pressure wind tunnel, revealing that wind loads significantly influenced mechanical performance and tracking precision. These findings highlight the importance of understanding wind loads for designing heliostats capable of maintaining accurate solar tracking under adverse wind conditions. Wind significantly affects the mechanical performance of heliostats, as forces transmitted through the drive mechanisms are directly influenced by wind direction, speed, and turbulence intensity (Emes *et al*., 2015). Additionally, optimizing heliostat field layout is crucial to minimizing wind-induced vibrations and displacements, which can cause optical errors, particularly under turbulent conditions (Bendjebbas *et al*., 2016). Yang *et al*. (2022) proposed an umbrella support structure for heliostats to enhance mechanical stability, especially under wind loads. Compared to traditional designs, this structure offered a 17.7% cost saving with negligible loss in optical efficiency. Forman *et al*. (2025) analyzed a lightweight, modular heliostat made from high-performance concrete.

A major challenge in heliostat design is preventing wind-induced vibrations from degrading the optical performance of the mirrors. Wind can cause the mirrors to vibrate, potentially leading to tracking errors that reduce the efficiency of the CSP system. In extreme cases, high wind speeds can cause mechanical failure of heliostat components (Sun *et al*., 2014). Therefore, developing heliostat designs that can withstand these forces while minimizing their impact on optical accuracy is crucial. Several studies have shown that reducing the size of heliostats or adjusting their orientation relative to the wind can help mitigate these effects. For instance, Jafari (2020) found that turbulence from upstream heliostats could significantly affect the wind loads on downstream heliostats in a CSP field. The study also suggested that adjusting heliostat layouts and incorporating windbreaks, such as perimeter fences, could help reduce wind loads and enhance system stability. Ji *et al*. (2023) proposed an evaluation method to assess the impact of wind loads on the concentrating efficiency of heliostats with multiple sub-mirrors. The study evaluated concentrating efficiency under varying pitch angles and wind directions, finding that wind-induced vibrations reduced the heliostat's efficiency from 95.5% to 72.2%.

Recent studies have increasingly focused on optimizing heliostat design to address the dynamic nature of wind forces. Emes *et al*. (2020) and Merarda *et al*. (2020) conducted research correlating turbulence data from the atmospheric boundary layer (ABL) with wind load coefficients obtained from wind tunnel experiments. Their studies emphasized the influence of terrain roughness and turbulence intensity on wind load profiles. For instance, Emes *et al*. (2020) found that larger heliostats in rougher terrain required greater structural mass to withstand higher wind loads, leading to increased material costs. This underscores the need for heliostat designs tailored to specific site conditions to optimize both performance and cost. Factors such as the mirror aspect ratio, the size and weight of the supporting frame, and the configuration of the drive mechanisms must all be carefully considered to account for the unique wind conditions at each site.

Wind tunnel testing has been a key method for analyzing wind flow patterns and their effects on heliostat performance (Peterka & Derickson, 1992; Blume *et al*., 2023). However, the complex, turbulent nature of wind and the varying geometries of heliostats present significant challenges for accurate modeling and prediction. Emes *et al*. (2024) explored the effects of ABL turbulence on aerodynamic wind loads on a heliostat, comparing field measurements with wind tunnel experiments. Two studies were conducted: one with field measurements at the ABL research facility and the other with wind tunnel tests on a scale model heliostat. The results revealed that wind tunnel experiments overestimated drag force coefficients and underestimated lift force coefficients compared to field measurements. This highlighted the importance of incorporating ABL turbulence characteristics for more accurate aerodynamic load predictions on heliostats. Marano *et al*. (2024) investigated the impact of facet gaps on wind loads in multi-facet heliostats through experimental testing in a large wind tunnel. Their findings showed that introducing a gap between facets generally increased wind loads, with larger facet aspect ratios amplifying the effect. The gap caused shifts in the maximum load cases, impacting lift force, hinge moment, and azimuthal moment coefficients, which could affect tracking accuracy and overall performance of CSP plants. Bakhshipour *et al.* (2024) examined the influence of heliostat aspect ratio (AR) and ground clearance ratio (GR) on static wind load coefficients through wind tunnel experiments. Their experiments measured forces and moments on heliostat models with five different ARs (ranging from 1 to 2) and four different pylon hinge heights (0.1<GR<1) at various elevation angles. The results indicated that increasing AR had minimal effect on drag and lift coefficients but increased hinge and overturning moment coefficients by up to 55% compared to a square heliostat. For constant GR, increasing AR reduced drag and overturning moment coefficients, as well as lift coefficients for AR?1.5. The effects of GR showed that drag coefficients remained constant, while lift coefficients increased slightly. Higher GR values led to a rise in overturning and hinge moment coefficients by up to 40% and 30%, respectively. Additionally, increasing hinge height resulted in higher lift, overturning moment, and hinge moment coefficients.

The aerodynamic performance of heliostats under different wind conditions is influenced by factors such as mirror shape, tilt angle, and orientation. Merarda *et al.* (2020) examined the effect of mirror shape on aerodynamic loading through wind tunnel tests under both smooth and turbulent flow conditions. Three mirror shapes-square, octagonal, and circular-were tested at different turbulence intensities. The findings indicated that, in smooth flow, the mirror shape had a minimal impact on mean force coefficients but influenced the fluctuating aerodynamic loads. In turbulent conditions, the circular mirror shape was found advantageous for the aerodynamic design of the elevation drive and mirror support structure, reducing aerodynamic loading. Fadlallah *et al.* (2021) explored the impact of wind incidence angles on aerodynamic loading using computational fluid dynamics (CFD) to better understand how wind flow characteristics influence wind loads. The results, validated by wind tunnel data, revealed that both tilt and wind incidence angles significantly impacted aerodynamic coefficients. The study also provided a comprehensive analysis of lift, drag, overturning, and hinge moment coefficients, along with generalized correlations based on heliostat orientation. These insights offer valuable tools for evaluating structural loads in heliostat designs. Understanding the interaction of these variables is crucial for developing heliostat designs that are both structurally sound and optically efficient under varying wind conditions.

One promising area of research is the use of computational fluid dynamics (CFD), large eddy simulations (LES) and direct numerical simulation (DNS) to model wind-induced forces on heliostats. These advanced computational techniques enable more accurate and detailed simulations of wind flows and their effects on heliostat performance, reducing the need for costly physical wind tunnel testing (Ji *et al.*, 2023; Li *et al.*, 2024; Hamidi, M. S., 2024). By simulating wind loads on heliostat components, researchers can identify structural weaknesses and optimize designs to minimize wind-induced stress, enhance tracking accuracy, and reduce optical errors. Sosa-Flores et al. (2022) studied how rear geometry influences the aerodynamic load coefficients of heliostats in the stow position, which is crucial for designing and estimating the costs of concentrated solar thermal power tower plants. Using LES, they analyzed how different rear geometries of a squared heliostat affected hinge moments, drag, lift, and overturning coefficients. Li *et al.* (2024) examined the use of LES to evaluate wind loads on ground-mounted heliostat trackers, focusing on the effects of geometric details and near-ground turbulence. Their findings showed that LES accurately replicated integral force coefficients and local pressure distributions. The study revealed that support components contribute more than 50% to the mean lift and overturning moment in stow positions and clarified how turbulence intensity and length scale influence the wind load design, establishing a foundation for LES applications in heliostat arrays. Merarda *et al.* (2024) analyzed heliostat fatigue across six regions of Algeria, focusing on the impact of wind speed distribution. Using CFD and FEA simulations, they assessed wind loads, structural performance, and resistance to wind-induced stresses. Their study demonstrated that regions with higher wind speeds experience greater stress concentrations, reducing heliostat lifespan and increasing maintenance costs. This underscores the need to consider long-term wind load effects when designing heliostats, especially in areas with high wind exposure. Ali and Jifeng (2024) applied computational wind engineering (CWE) to assess the wind effects on tower heliostats in solar thermal power stations, focusing on deflection, deformation, and potential collapse. They developed three mathematical models for inlet boundary conditions and used user-defined functions (UDF) to simulate wind tunnel conditions. They calculated wind load coefficients and identified optimal heliostat spacing to prevent mechanical collisions and shielding losses, offering guidelines for wind-resistant heliostat design and layout optimization in windy and sandy environments.

Reducing the costs of heliostats and enhancing their structural performance under wind loads are crucial for the successful implementation of CSP technology. Continued research into wind load effects, heliostat design optimization, and field layout configurations will be crucial for lowering the levelized cost of electricity (LCOE) and making CSP a more economically competitive energy source. This study aims to advance that understanding by modelling and analyzing the wind loading effects on heliostat mirrors using computational fluid dynamics (CFD). In this work, a comprehensive CFD study of heliostats is conducted to investigate the flow behavior over the heliostat surface at various elevation angles using local (UET Lahore campus) environmental data for its indigenous development and deployment of a functional prototype, which has never been done in the past research. This approach will provide valuable insights into optimizing heliostat designs for both structural integrity and optical performance, paving the way for more cost-effective and reliable CSP systems.

2. Methodology

The CFD problem formulation and solution process includes geometric modelling of the heliostat assembly in CAD software, mesh generation, boundary conditions, numerical solution, and post-processing of the data (Natraj *et al.*, 2021; Yu *et al.*, 2019). In this study, the wind aerodynamic behavior over the heliostat surfaces at various elevation angles was analyzed through three dimensional (3D) CFD simulations.

2.1. Geometric Modeling

In the CFD modeling process, the first step is to develop a CAD model of the entire heliostat structure. The chosen design consists of two reflectors mounted on a common horizontal shaft, allowing for combined motion. A slew drive rotates this shaft to adjust the inclination of the heliostat reflectors. A vertical pole, known as the pedestal, supports the entire assembly and allows for vertical rotation to achieve the desired azimuth angle. The width and length of each heliostat reflector are 1.0058m (3.3ft) and 2.01168m (6.6ft), respectively, giving a total reflector area of 2.13m^2 (21.78 ft^2). The pedestal height is set at 0.6096m (5.5ft) to allow for the constraint free rotation of the assembly.

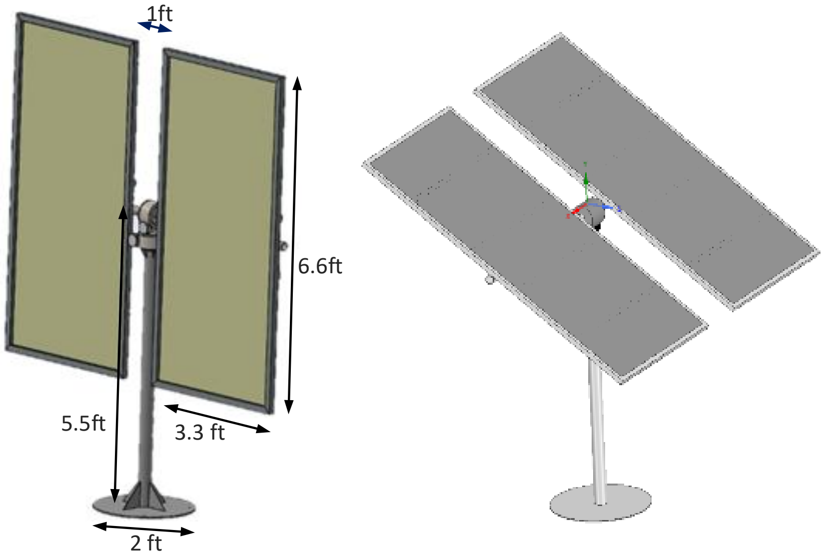

Fig 1. (a) CAD model of heliostat with specifications, (b) CAD model assembly as single entity for CFD analysis

The complete geometric specifications of the heliostat, as developed in SolidWorks, are shown in Figure 1 (a). This CAD model was then defined as a single geometric model for export to ANSYS for further analysis, as shown in Figure 1 (b). The model allows for the degree of freedom for both azimuth and inclination of the heliostat reflectors. This adequate CAD modelling serves as a precursor to the computational fluid dynamics (CFD) analysis of heliostat to examine the wind load, wind pressure, and velocity distribution on the heliostat surface.

2.2. Computational Domain and Meshing

The development of the physical 3D model and computational domain is a crucial step in CFD analysis. The size of the computational domain in the Cartesian coordinate system depends on the model's geometric dimensions and the boundary conditions used for analysis (Martín *et al*., 2016; Mughal *et al*., 2022). In this simulation, based on full-scale geometric dimensions, the inlet side was set to $5W$ (five times the width of the heliostat), and the top side was set to $6H$ (six times the height of the heliostat). The outflow side was taken as $5W$ (five times the length of the heliostat). These dimensions of the computational domain follow recommendations to ensure that the domain envelop has a negligible effect on the computational parameters such as pressure and velocity fields. A complete view of the computational domain, along with its geometric specifications, is shown in Fig 2.

For the computational domain, a multi-block (mixed grid division) method was used to accurately define the grid. The mesh grid was developed to meet specific requirements, including mesh type, size, and refinement levels around the heliostat assembly. **Error! Reference source not found.**illustrates the developed domain grid, which consists of 1,750,000 cells, along with the skewness of the computational grid. The minimum and maximum skewness values are 0.04 and 0.548, respectively, which are considered adequate for the developed grid cells (Waqas & Ahmad, 2020; Mughal *et al*., 2022). The computational domain grid and its skewness are shown in **Error! Reference source not found.**(a & b).

2.3. Governing equations and boundary conditions

The primary equation governing the computational fluid dynamics is based on the Navier-Stokes equation, which includes the mathematical relations for the conservation of mass, momentum, and energy (Waqas & Ahmad, 2020; Mughal *et al*., 2022). The conservation of energy was not considered in this analysis, as temperature variations were not a primary focus of

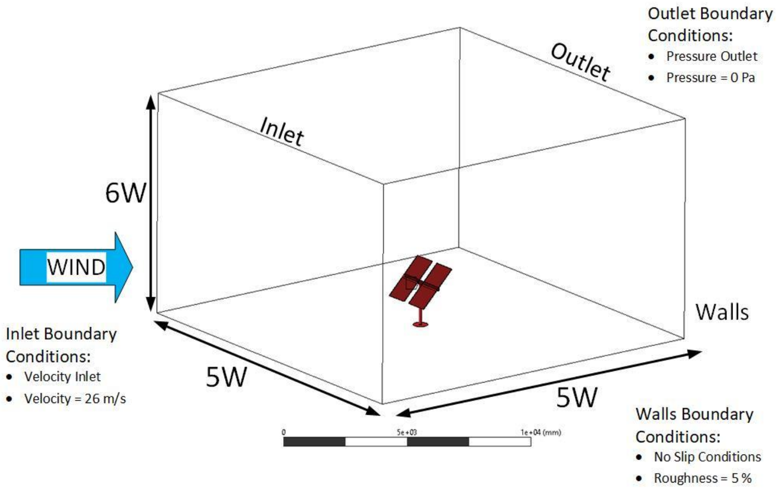

Fig 2. Computational Domain for Heliostat CFD Analysis

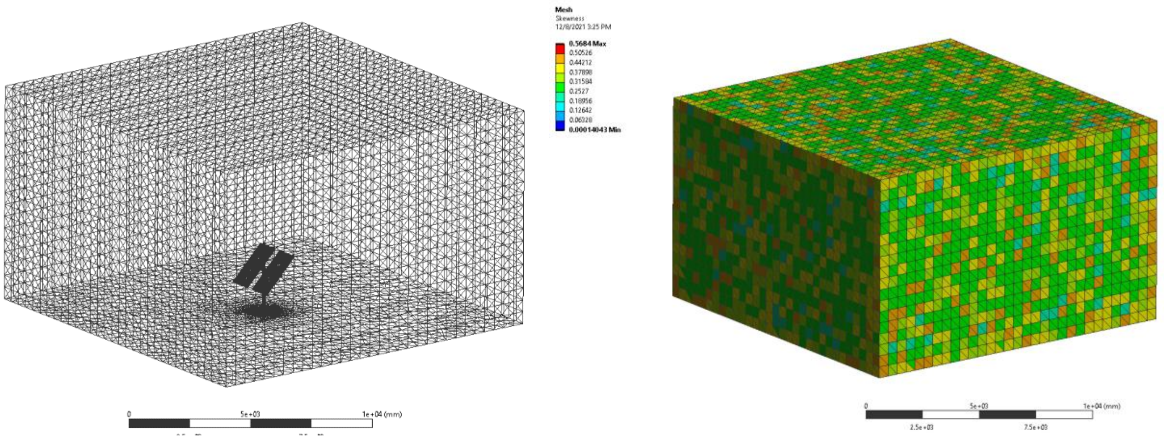

Fig 3. Computational Domain Grid (a), Computational Grid Skewness (b)

investigations. In the Cartesian coordinate system, the Navier-Stokes equation in terms of air velocity u, density ρ and pressure p can be written as:

$$\frac{\partial}{\partial x_i}(\rho\, u_i) = 0 \tag{1}$$

$$\frac{\partial}{\partial x_i}(\rho\, u_i\, u_j) = \frac{\partial p}{\partial x_i} + \frac{\partial}{\partial x_j}\left[\mu\left(\frac{\partial u_i}{\partial x_j} + \frac{\partial u_j}{\partial x_i}\right)\right] + \frac{\partial \tau_{ij}}{\partial x_j} \tag{2}$$

In present research, the standard k-ε was used which is well-suited for simulating turbulent flows in wall-bounded regions, typical in wind loading scenarios where boundary layers near the mirrors significantly influence aerodynamic forces. It is computationally less intensive than more complex models like the Reynolds Stress Model (RSM) or Large Eddy Simulation (LES), which, though more accurate, demand much greater computational resources to capture every minute detail of turbulence. The RNG k-ε model offers enhanced accuracy for flows with strong curvature or high strain rates, but its added complexity and computational cost may not provide substantial benefits for the specific flow characteristics of heliostat mirrors. The k-ω model, while effective for near-wall flows, is more sensitive to boundary conditions and requires finer meshing, making it less practical for large-scale studies. The standard k-ε model has been widely validated for similar wind loading applications, ensuring its reliability for this study due to robustness in execution, adequate precision and low computational burden (Emes *et al*., 2024; Mughal *et al*. 2022; Abd Halim *et al*., 2018; Mahfoud *et al*., 2013). This model consists of two mathematical expressions: one based on turbulent kinetic energy and the other on the dissipation rate. The equations are provided by Eq 3 and 4.

$$\frac{\partial}{\partial x_i}(\rho k) + \frac{\partial (p u_i k)}{\partial x_i} = \frac{\partial}{\partial x_j}\left[\left(\mu + \frac{\mu_t}{\sigma_k}\right)\frac{\partial k}{\partial x_j}\right] + G_k - \rho\varepsilon + G \tag{3}$$

$$\begin{aligned}\frac{\partial}{\partial x_t}(\rho\varepsilon) + \frac{\partial (p u_i \varepsilon)}{\partial x_i} \\ &= \frac{\partial}{\partial x_j}\left[\left(\mu + \frac{\mu_t}{\sigma_\varepsilon}\right)\frac{\partial \varepsilon}{\partial x_j}\right] \\ &+ C_{1\varepsilon}\frac{\varepsilon}{k}(G_k + C_{3\varepsilon}G_b) - C_{2\varepsilon}\rho\frac{\varepsilon^2}{k}\end{aligned} \tag{4}$$

Here μ and μ_t are the laminar and turbulent viscosities, repectively, whereas the terms G_k, G_b denotes the generation of the turbulent kinetic energy, respectively, due to fluid's velocity gradient and resistance. These terms are defined as follows:

$$G_k = -\rho\overline{u_i' u_j'}\frac{\partial u_j}{\partial x_i} \tag{5}$$

$$G_b = -g_i\frac{\mu}{\rho\sigma_h}\frac{\partial \rho}{\partial x_i} \tag{6}$$

In these relations $C_{1\varepsilon} = 1.44$, $C_{2\varepsilon} = 1.92$ and $C_{3\varepsilon} = 1.8$ are constant. The turbulent Prandtl numbers for k and ε are $\sigma_k = 1.0$ and $\sigma_\varepsilon = 1.3$. The viscosity μ_t can be determined from the following relation.

$$\mu_t = C_\mu k^2/\varepsilon \tag{7}$$

To initiate the computational solution, boundary conditions are imposed on the outer surface of computational domain and geometrical surfaces of 3D heliostat model as shown in Figure 2. A constant wind velocity of $26\,m/s$, representing the average wind speed at heliostat installations, is applied at the inlet of the computational domain, while ambient pressure is applied at the outlet. The incoming wind at the entrance of the computational domain is modelled using a power-law velocity profile, as in Equation (8), which represents wind speed variations within the atmospheric boundary layer (ABL). This profile accounts for the increase in wind speed u with height h, simulating the shear effects near the ground. It provides a more realistic representation of wind conditions at heliostat installations, where wind speed typically increases with height due to roughness surface. The power-law profile inherently considers ABL effects, which are critical when simulating wind loading on heliostat structures. Symmetrical boundary conditions are applied to the side walls and top surface of the computational domain, modelled as free-slip surfaces in viscous flow. This means no shear stress is applied at the boundaries, and the flow is assumed to be symmetric and undisturbed at these surfaces. Heliostat collector surfaces and ground surfaces in computational domain are declared as non-slipping surfaces. The outflow boundary condition is set to ambient pressure at the domain exit, preventing backflow and ensuring natural flow exit. While wake effects behind the heliostat are not modelled in detail at the exit, the domain is sufficiently large to minimize the outlet

Table 1
Material properties of heliostat reflector

Elastic modulus $[GPa]$	Poisson's ratio	**Density** $[kg/m^3]$	**Yield strength** $[MPa]$
210	0.27	7850	310

boundary's influence on wake development. Using ambient pressure at the exit prevents interference with the wake and ensures a realistic flow field in the region of interest.

$$\frac{u}{u_r} = \left[\frac{h}{h_r}\right]^{0.15} \tag{8}$$

The heliostat mirrors were constructed using highly reflective steel sheets, while the frame and pedestal were made of structural steel, with the mechanical properties listed in Table 1.

2.4. Numerical solution and mesh convergence

The numerical solution setup involves several steps. In the first step, forced convection of the fluid was considered in the computational setup. Nodes and cells define the control volume in the discretized model of the entire computational domain. At each control volume, the residuals of the momentum, turbulence, and discretized continuity equations were calculated, and the velocity convergence was checked. For the steady-state analysis, a second-order implicit time formulation and Green-Gauss cell-based method were chosen for better numerical solution accuracy. A residual value of 10^{-5} was selected to ensure convergence of the numerical solution.

The computational numerical solution determines the physical parameters at each mesh node. The computational burden on the processor depends on the number of nodes in the mesh of the entire geometry. A mesh independence study is crucial for understanding both the computational overhead and the accuracy of the solution. This study was conducted at various levels of mesh refinement while computing grid convergence index (GCI) until no significant variations were observed in the results (GCI < 2%). The key computed variables, such as maximum turbulent kinetic energy, maximum static pressure, lift force, drag force and maximum velocity, were evaluated at different mesh refinement levels. The initial mesh for this problem contained 1,571,832 elements and 284,569 nodes. The meshing parameters, including skewness, aspect ratio, and average orthogonal quality, were 0.25, 1.84, and 0.81, respectively. These parameters were examined to fall within the appropriate and acceptable range (Waqas & Ahmad, 2020). Figure 4 (a-d) illustrates the variation in maximum turbulent kinetic energy, maximum static pressure, lift force and drag force at different mesh refinement levels.

2.5. Forces and moments on heliostat

Heliostats are typically installed in open spaces, where structural and operational robustness are crucial for sustained and accurate performance. The system's overall integrity must be sufficient to withstand various environmental factors, such as wind, extreme temperatures, rain, and humidity. Among these, the forces and moments induced by wind are the most significant in affecting the heliostat's structural and operational reliability.

To analyze the forces and moments acting on the heliostat, the coordinate system is established for vector analysis. The longitudinal x-axis is aligned with the airflow direction. Perpendicular to the x-axis, the y-axis is defined in the lateral direction, whereas z-axis is defined in the vertical direction. The forces acting along the x, y, and z axes correspond to the drag forces ($F_D = F_x$), sway forces, and lift forces ($F_L = F_z$),

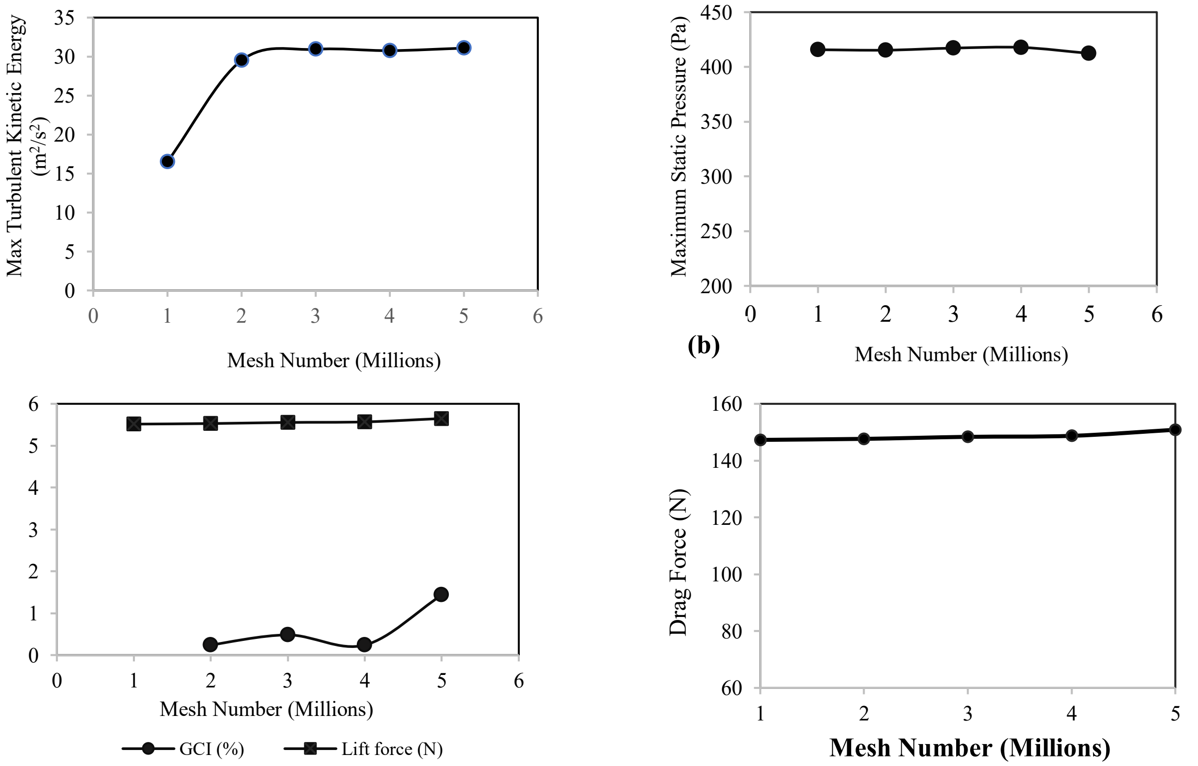

Fig 4. Variation of a) maximum turbulent kinetic energy, b) maximum static pressure, c) lift force and GCI, d) drag force with different mesh refinement levels

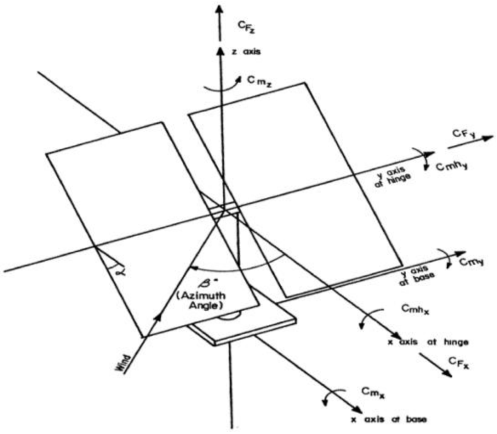

Fig 5.The Coordinate system, forces and moments acting on heliostat (Peterka & Derickson, 1992)

respectively. Additionally, the moments acting about y-axis and z-axis are the overturning moment (M_y), hinge moment (M_{hy}) and azimuth moment (M_y), as shown in Figure 5. The following equations can be used to calculate various forces and moments acting on the heliostat.

$$
\begin{aligned}
F_x &= C_{Fx}\frac{1}{2}\rho U^2 A \\
F_z &= C_{Fz}\frac{1}{2}\rho U^2 A \\
M_{hy} &= C_{Mhy}\frac{1}{2}\rho U^2 A Z_m \\
M_z &= C_{Mz}\frac{1}{2}\rho U^2 A Z_h \\
M_y &= C_{My}\frac{1}{2}\rho U^2 A Z_h
\end{aligned}
\tag{9}
$$

Here C_{Fx}, C_{Fy}, C_{Mhy}, C_{Mz} and C_{My} are the wind load co-efficients, A is the heliostat area, U is average wind speed, whereas Z_h and Z_m represent the heights of elevation axis and mirror plane, respectively.

3. Results and discussions

The CFD model of the heliostat system was set up for simulation, and the numerical simulations were performed for various operating modes. Boundary conditions were applied as previously described in Section 2.2. The numerical solution provided average wind pressure on the heliostat surface, as well as force and moment coefficients. Additionally, the streamlines were analyzed to examine wind pressure distribution over the heliostat surface and the characteristics of the flow field. Other parameters, such as dynamic pressure, turbulent kinetic energy, turbulence intensity, and skin friction effects, were also computed for analysis. Four different operating modes of the heliostat at various elevation angles, 0°, 30°, 60° and 90°, were considered in the simulation, as shown in Figure 6. The horizontal position was taken as the reference position, with a slope angle of zero degree. The heliostat was then rotated about the y-axis to establish the other orientations, with the vertical position finally being set at 90°.

3.1. Analysis of streamlines, velocity magnitude and turbulence intensity

The fluid flow behaviour over the heliostat surface at various elevation angles was investigated through the solution of a validated CFD model. Figure 7 displays the side view of the heliostat system, illustrating the distribution of streamlines,

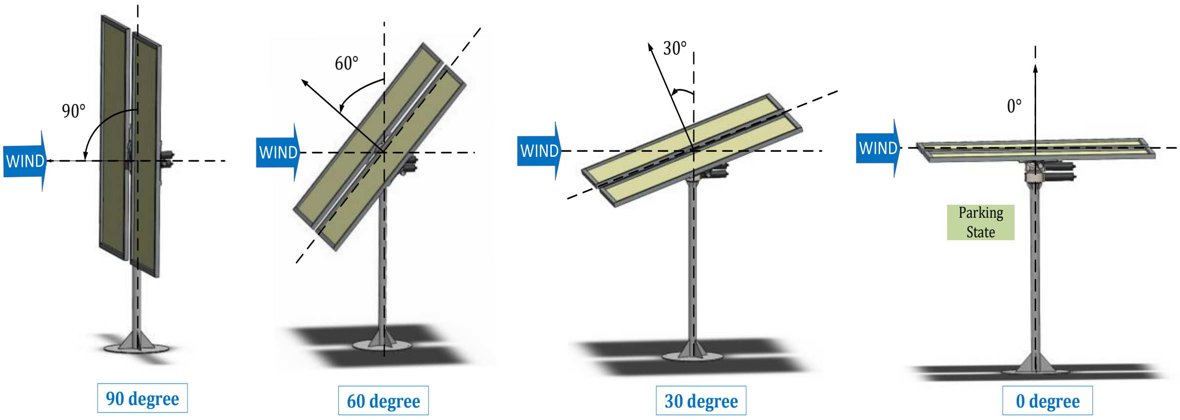

Figure 6: Heliostat Operating Positions

velocity fields, and turbulent kinetic energy. The results clearly indicate the formation of turbulence on the leeward side of the heliostat, which arises as the incoming airflow interacts with the mirror surface. This turbulence is predominantly driven by the instability and periodic shedding of shear layers, generated at the flow separation points along the upper and lower edges of the mirror. Figure 8 presents the airflow behaviour over the heliostat system observed from the top view. Increasing the elevation angle significantly impacts downstream vortex formation.

Understanding the aerodynamic behaviour and load distribution on the heliostat is crucial to predict potential failures and structural damage. Analysing the flow characteristics predicted by the computational models offers valuable insights into these aerodynamic effects. The key parameters such as streamlines, velocity fields, and turbulence levels were examined, as they reveal vortex core regions and wind speed variations at different elevation angles. Figures 7 and 8 present side and top views to visualize the three-dimensional turbulent flow structures around the heliostat.

The comparative analysis of streamlines near the heliostat at various elevation angles (0°, 30°, 60°, and 90°) provides a qualitative assessment of the CFD model's ability to replicate the flow behavior around the structure. The vortex formation is a primary contributor to the fluctuating drag and lift forces acting on the heliostat, which can induce structural stresses and potential damage (Mahfoud *et al.*, 2022). The numerical results

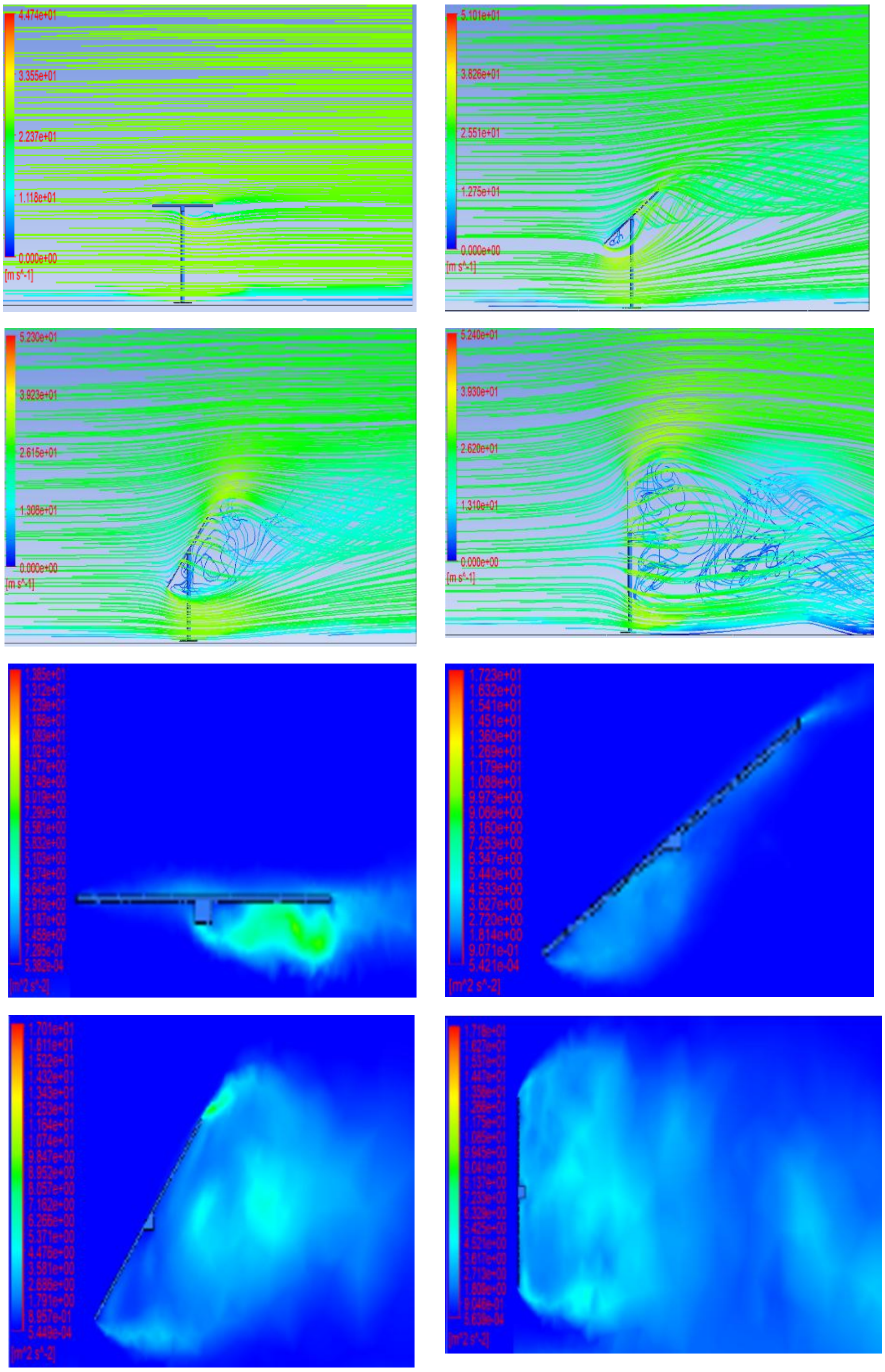

Fig 7. Flow streamlines, flow velocity and turbulent kinetic energy for various elevation angles of heliostat (side view)

capture the downstream recirculation zones appropriately, including vortices, as illustrated in Figures 7 and 8.

The side view shown in Figures 7 highlights the vortex development mechanism as wind flows over the heliostat surface. The airflow accelerates and generates turbulence on the leeward side, driven by the interaction of separating shear layers, which leads to periodic vortex shedding. This phenomenon is absent when the heliostat is in the horizontal position ($\alpha = 0°$). Near the ground, at operating angles of 30°, 60°, and 90°, the wind flow pattern is entirely different; the lower shear layer is either weakened or suppressed, preventing the interaction between separated flows downstream. The flow separation and reattachment points are distinctly observable, with reattachment locations more precisely identified in this view.

Decreasing the elevation angle from 90° to 0° results in a noticeable reduction in the size of the downstream vortex. The wind velocity measurements indicate the lowest speeds adjacent to the windward and leeward surfaces for angles 90°, 60°, and 30°, whereas maximum velocities occur near the trailing edge of the heliostat. Additionally, the wind velocity above the heliostat decreases with the elevation angle.

To provide a more comprehensive understanding of the wind behaviour around the heliostat, turbulent kinetic energy distributions at the selected elevation angles are presented in Figures 7 and 8. These contours offer insight into the aerodynamic environment surrounding the heliostat structure for various orientations. The CFD analysis reveals that the elevated turbulence levels predominantly occur on the leeward side of the heliostat. This is attributed to the formation of recirculation zones, which are clearly identified in the corresponding streamline patterns. Such zones are typical behind bluff bodies and are known to induce flow separation and turbulent wake regions. Conversely, a marked reduction in the turbulent kinetic energy, hence turbulence intensity is observed

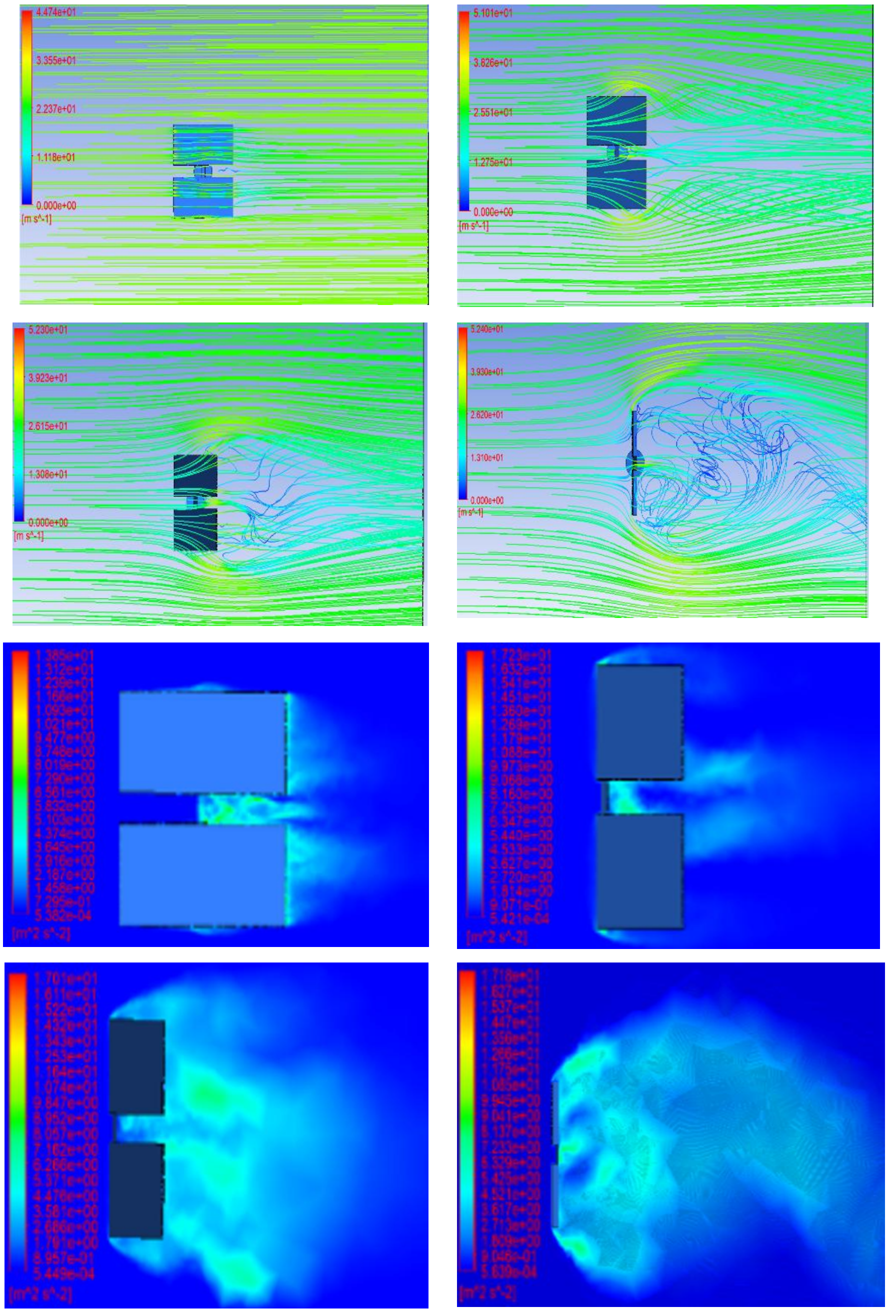

Fig 8. Flow streamlines, velocity and turbulence kinetic energy for various elevation angles of heliostat

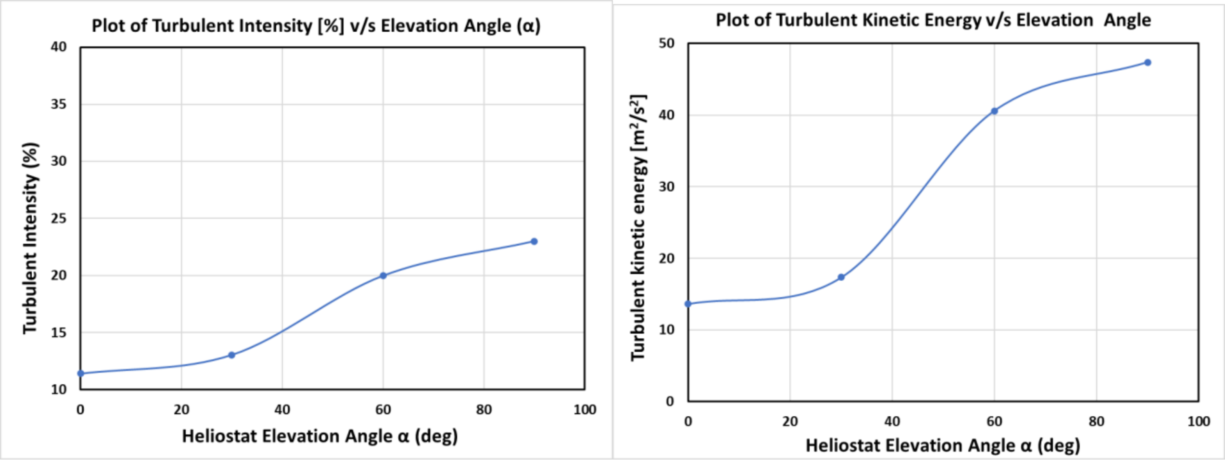

Fig 9 Variation of (a) turbulence intensity and (b) turbulent kinetic energy at various heliostat elevation

on the windward side as the elevation angle of the heliostat decreases from 90° to 0°. This trend is likely due to the reduction in the frontal surface area directly facing the wind flow, which in turn minimizes the flow disruption and reduces the generation of upstream turbulence. The correlation between increased elevation angle and reduced windward turbulence emphasizes the importance of tilt orientation in heliostat aerodynamic performance.

The integrated analysis of Figures 7 and 8 allows for a three-dimensional interpretation of the complex, unsteady flow structures that develop around the heliostat under varying operating conditions. These results highlight the formation of vortex cores, recirculation zones, and regions of flow acceleration, which together influence the fluctuating aerodynamic forces acting on the structure. Such detailed flow characterization is vital for optimizing heliostat design to ensure aerodynamic stability, structural resilience, and energy efficiency in large-scale concentrated solar power plants.

Furthermore, the turbulence intensity on the heliostat was examined and found to increase as the elevation angle increased. The variation in turbulence intensity at different elevation angles is shown in Figure 9. The minimum and maximum turbulence intensity values were 23.01% and 11.42%, observed at elevation angles of 0° and 90°, respectively. It is also evident that the turbulent kinetic energy increased with the elevation angle. The minimum value of turbulent kinetic energy was found to be 13.65 m^2/s^2 at anelevation angle of 0°, which is notably lower compared to the values at 90°. These results were found to be in accordance with the findings of Mahfoud et al. (2022) and Bakhshipour et al. (2025). The nonlinear trends in the graphical representations of turbulence intensity and turbulent kinetic energy result from the nonlinear impact of airflow on the heliostat surface at different elevation angles. Turbulent kinetic energy and turbulence intensity are critical factors in assessing wind loading on heliostats. High turbulence, especially at certain angles, can induce fluctuating aerodynamic forces that may lead to structural oscillations. Over time, these oscillations could contribute to fatigue damage, particularly at points of high stress, such as the connections between the reflector and supporting structure. Understanding these turbulence characteristics helps to predict potential issues with heliostat stability and improve the design to ensure durability under varying wind conditions.

3.2. Analysis of lift and drag forces on heliostat surface.

The impact of different elevation angles on the aerodynamic performance characteristics of the heliostat was investigated using CFD and presented in Table 2. As the elevation angle increases, the drag force rises substantially, indicating greater wind resistance due to increased frontal exposure. The lift coefficient peaks at 30°, suggesting strong asymmetric flow separation at this angle. The dynamic pressure and turbulence intensity also increase with the elevation angle, reflecting enhanced wake and vortex formation. In contrast, the skin friction coefficient does not increase substantially, indicating pressure forces dominate. These results highlight the sensitivity of heliostat aerodynamics to tilt angle and the need for careful orientation to minimize losses and structural damage.

Additionally, the graphical representation of the drag coefficient, drag force, lift coefficient, and lift force is shown in Figure 10. It is evident that both the drag coefficient and drag force increase as the heliostat elevation angles rise. This increasing trend is due to the increased impact of air on the heliostat surface. The maximum and minimum drag coefficient

Table 2
Aerodynamics performance parameters of heliostat

Performance Parameters	$\alpha = 0°$	$\alpha = 30°$	$\alpha = 60°$	$\alpha = 90°$	**Standard Deviation**
Drag Coefficient (C_D)	0.3580	2.6097	3.3961	4.1043	1.41
Drag Force F_D (N)	148.23	1080.5	1405.2	1604.92	558.53
Lift Coefficient (C_L)	0.0134	4.3796	3.3088	0.0852	1.94
Static Pressure [Pa]	418.60	428.46	437.89	468.87	18.84
Dynamic Pressure [Pa]	1328.3	1773.3	3905.7	4687.73	1409.33
Skin Friction Coefficient	0.0111	0.0133	0.0133	0.0139	0.00
Turbulence intensity [%]	11.42	13.06	19.99	23.01	4.79

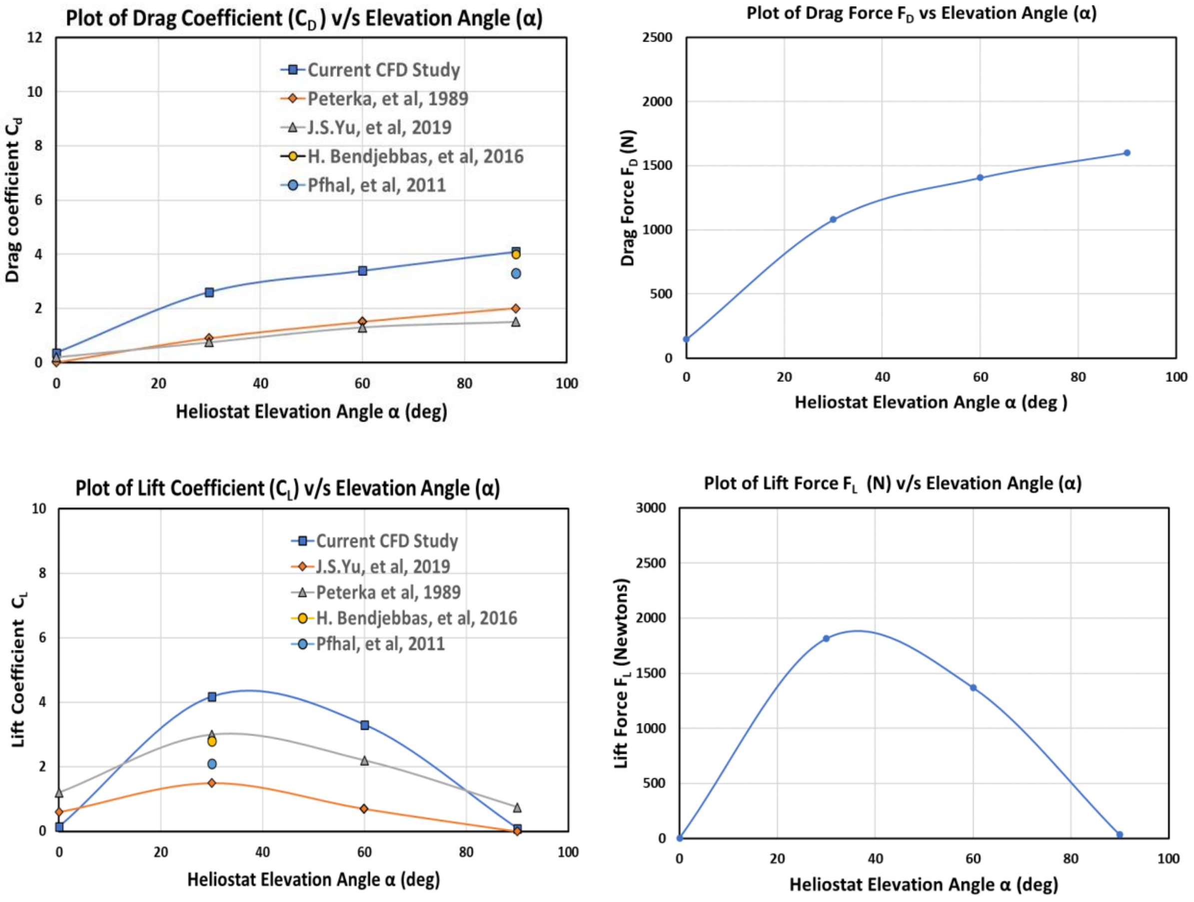

Fig 10 Variation of drag coefficient, drag force, lift coefficient and lift force at different heliostat elevation angles.

values were recorded as 4.1043 and 0.3580 at elevation angles of 90° and 0°, respectively. The drag coefficient is validated against experimental data from Peterka *et al.* (1989) and Yu *et al.* (2019). The discrepancies between predicted and experimental values are attributed to the numerical solution quantization errors and unmodeled dynamics in the model. The results also show that the maximum and minimum drag force values occur at elevation angles of 90° and 0°, respectively. The trend for the lift coefficient and lift force initially increases to a certain point and then decreases. The minimum and maximum lift coefficient values were observed to be 0.0134 and 4.3796 at elevation angles of 0° and 30°, respectively, and were validated against experimental results from Peterka *et al.* (1989) and Yu *et al.* (2019). Furthermore, the minimum and maximum lift force values were observed to be 5.55 N and 1813.38 N at elevation angles of 0° and 30° respectively. The increasing trend of these coefficients is also reported by Bendjebbas *et al.* (2016) and Pfahl *et al.* (2011).

The observed trends in drag and lift forces can be attributed to the changing flow dynamics as the heliostat's elevation angle varies. The lift force peaks at 30° due to optimal interaction between the wind and the heliostat's surface, where the aerodynamic forces are maximized. After 30°, the lift force drops because the angle of attack increases, leading to flow separation from the surface, which reduces the effective lift. As the angle increases further, the airflow detaches more significantly, altering the aerodynamic behaviour and leading to an increase in drag force due to the larger surface area exposed to the wind. Flow separation and its effects on lift and drag are critical to understanding the heliostat's stability at different angles.

3.3. Effect of heliostat elevation angle on static and dynamic pressures

Figure 11 shows the pressure distribution around the heliostat for various elevation angles. At 90° elevation angle, the highest wind pressure was observed at the center of the windward face of the heliostat with low pressure near the corner. On the leeward side, a zone of negative pressure was formed, characterized by a more complex distribution due to aerodynamic interference from structural components. The region exhibiting the weakest negative pressure was observed just near the horizontal rotational axis. At elevation angles of 30° and 60°, the peak wind pressures tend to concentrate on the lower central portion of the mirror surface. For protection from extreme wind conditions, heliostats are rotated into a horizontal position ($\alpha = 0°$), thereby reducing the effective surface area exposed to wind loads and enhancing structural resilience.

The effect of different elevation angles i.e. 0°, 30°, 60° and 90° on static and dynamic pressures was examined using CFD results. Figure 12 (a-b) presents the predicted values of static and dynamic pressures at these elevation angles. The results clearly show that static pressure on the heliostat surface increases with

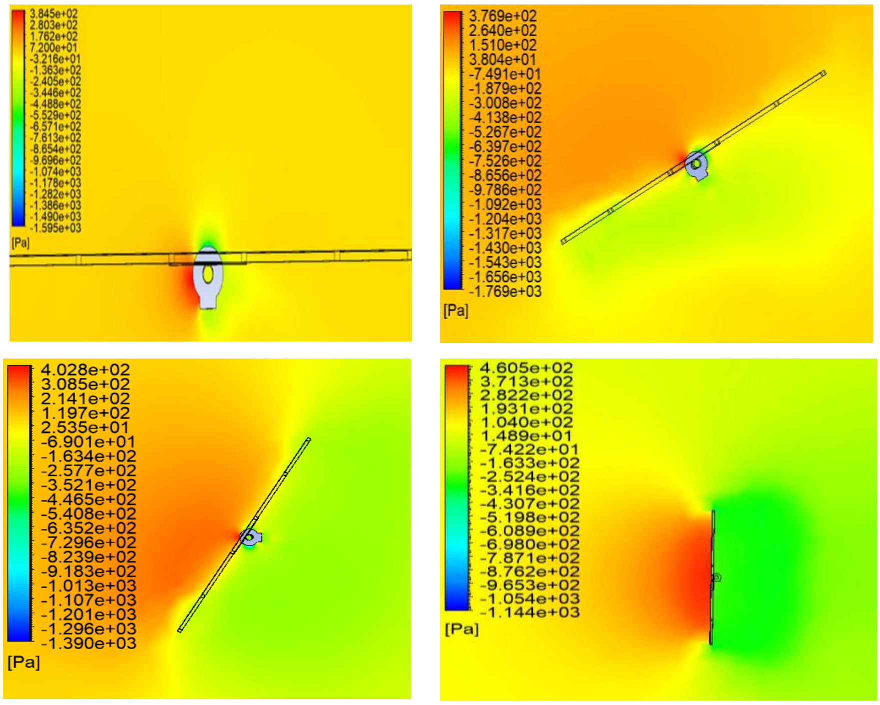

Fig 11. Pressure distribution around heliostat for various elevation angles

the elevation angle. The lowest static pressure occurs at a 0° elevation angle, due to the reduced impact of air at the horizontal position. Conversely, the highest static pressure is observed at the vertical position (90° elevation angle), where the air impact is greatest. The trend for dynamic pressure initially increases sharply up to an elevation angle of 60°, then rises more gradually at 90°. The maximum and minimum dynamic pressure values were found to be 4705.74 Pa and 1328.34 Pa at elevation angles of 90° and 0°, respectively.

Additionally, the graphical representations of the skin friction coefficient at different heliostat elevation angles are shown in Figure 12c. It is evident that the skin friction coefficient increases with the elevation angle. The maximum and minimum values of the skin friction coefficient were found to be 0.0139 and 0.0111 at elevation angles of 90° and 0°, respectively. These variations are attributed to the greater and less impact of air on the heliostat surface at higher and lower elevation angles.

To optimize heliostat designs and minimize wind-induced forces, several strategies can be employed. Adopting streamlined or curved mirror shapes can reduce drag by allowing smoother airflow over the reflective surface, thereby decreasing aerodynamic loads. Shapes like conical or parabolic mirrors could further enhance wind flow, minimizing high-pressure zones that contribute to excessive wind loads. Additionally, redesigning the support structures to be more aerodynamic, such as using tapered or triangular frames, can reduce the surface area exposed to wind and decrease drag. Implementing adjustable tilt mechanisms would allow heliostats to adapt to varying wind conditions, positioning the mirrors to avoid direct high-wind forces. Furthermore, the use of flexible materials for the frame and mirrors, along with the addition of damping systems, can absorb wind-induced forces and reduce structural fatigue. These design optimizations would effectively mitigate wind loads, enhancing the stability and longevity of heliostat systems in challenging environments.

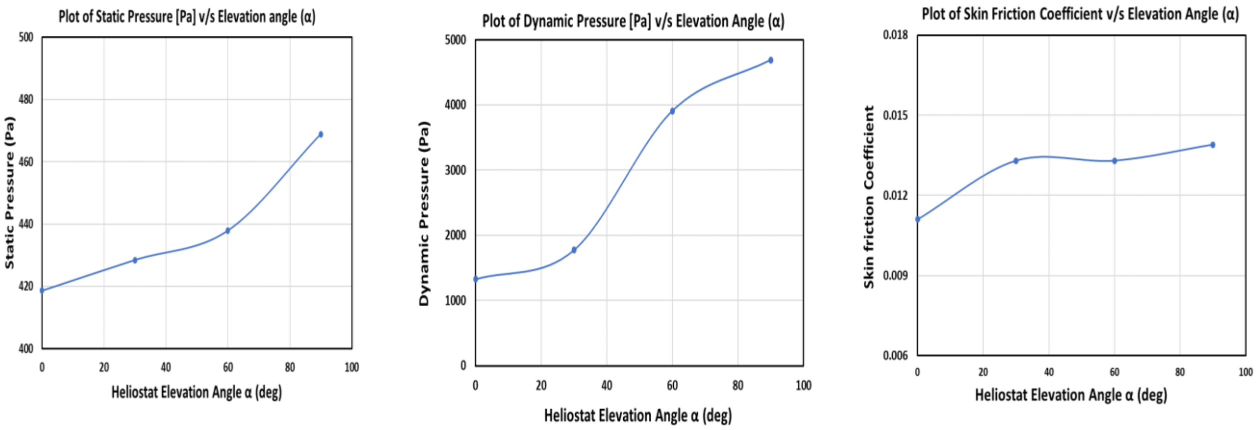

Fig 12. Variation of pressures and skin friction coefficient at various heliostat elevation angles

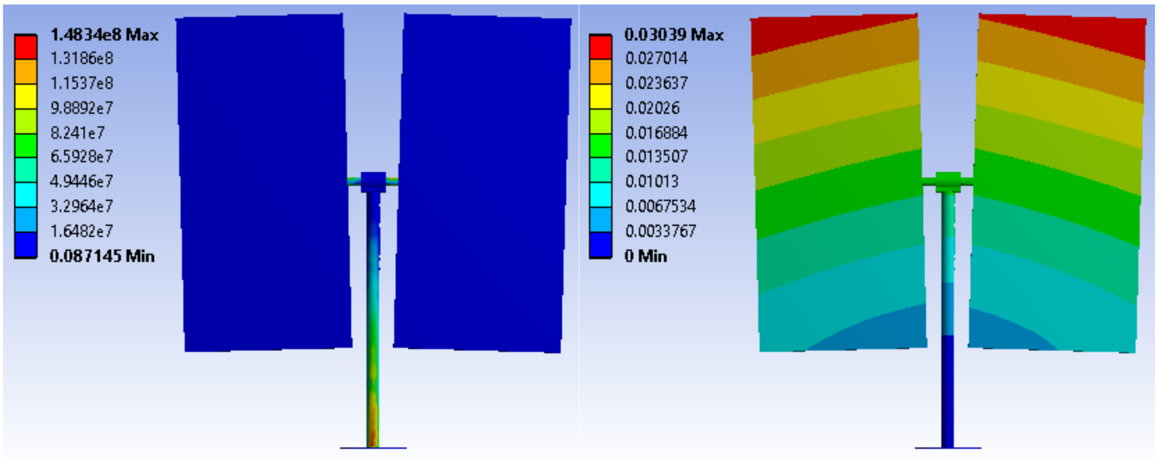

Fig 13. a) von Mises stress and b) deformation contour plots of the heliostat structure

3.4. *Finite element analysis of heliostat structural resistance to wind loading*

The finite element analysis (FEA) was performed using ANSYS to assess the mechanical response and resistance of the heliostat structure to the wind loading. The primary forces considered include wind load and gravitational loads on the heliostat structure that represent the dominant stress-inducing factors (Mahfoud *et al*., 2022). The most unfavorable condition was considered, with mirror panels oriented vertically ($\alpha = 90°$), either for maintenance or during certain tracking positions. The wind was assumed to act perpendicularly to the reflecting surface for that elevation angle. The stresses and deformations were found significantly less at other elevation angles.

The von Mises stress contour, presented in Figure 13a for an inclination angle of $\alpha = 90°$, reveals a maximum stress of $148.34\ MPa$, concentrated near the base of the pedestal. Importantly, this value remains within acceptable design limits with significantly lower stresses throughout the mirrors, indicating that the heliostat structure can safely withstand the wind loads. Minor stresses were observed in other components of the heliostat structure, indicating the pedestal as the critical structural member. The displacement results, shown in Figure 13b, indicate a maximum deflection of approximately 30.39 mm at the top edge of the heliostat. Considering the size of the heliostat mirror assembly, this level of displacement was found relatively small and unlikely to compromise system performance or tracking accuracy.

4. Conclusion

In this study, a three-dimensional Computational Fluid Dynamics (CFD) analysis was conducted to examine the flow behavior over the surfaces of heliostats at various elevation angles. Several key parameters, including drag and lift forces, drag and lift coefficients, static and dynamic pressures, skin friction coefficients, turbulent kinetic energy, and turbulence intensity, were investigated to evaluate the flow characteristics across the heliostat surface at different elevation angles.

The results revealed that drag and lift forces, as well as drag and lift coefficients, are strongly influenced by the elevation angle. At 0° elevation angle, these parameters exhibited their minimum values due to the reduced area of the heliostat exposed to the airflow. Similarly, static and dynamic pressures were found to be strongly dependent on the elevation angle, with lower values observed at lower elevation angles due to the smaller exposed surface area.

Additionally, the maximum and minimum values of the skin friction coefficient were 0.0139 and 0.0111 at elevation angles of 90° and 0°, respectively. The study also demonstrated that both turbulent kinetic energy and turbulence intensity are functions of the heliostat's elevation angle, with variations corresponding to the different aerodynamic impacts at each angle.

The finite element analysis confirmed that the heliostat structure can safely withstand the critical wind loads encountered during extreme operational scenarios. The stress and displacement levels remained within permissible limits, with the pedestal identified as the most critical component.

These findings provide valuable insights into the wind load behavior on heliostats and highlight the importance of elevation angle in optimizing heliostat design for improved structural performance and efficiency.

5. Future Recommendations

The primary goal of this research was to identify regions of high pressure, turbulence, and maximum velocity surrounding the heliostat surface under maximum wind conditions at local CSP installation site, which was successfully achieved through the CFD study. The future work could focus on conducting Fluid-Structure Interaction (FSI) analysis using ANSYS Workbench to investigate the heliostat's structural integrity and load-bearing capabilities in relation to wind loads on each surface. Additionally, structural design and material optimization present significant areas of interest, particularly in reducing the cost of heliostat fields. Consideration should also be given to the effects of vibrations and fatigue resulting from transient wind loads, which will be crucial for enhancing the durability and efficiency of heliostat systems.

Nomenclature:

x_i	Distance along x axis of Cartesian coordinate system
u_i	Velocity of air stream at distance x_i (m/s); $i = 1, 2, 3.$
ρ	Density of air (kg/m^3)
p	Pressure of fluid stream (Pa)
μ	laminar flow viscosity
μ_t	Turbulence viscosity, $kg/(m^2/s^2)$
G_k	Mean value of dynamic turbulence due to fluid speed
G_b	Mean value of dynamic turbulence due to fluid resistance
K	Turbulent kinetic energy

ε	Rate of dissipation of turbulent kinetic energy
σ_k	Turbulent Prandtl number for k
σ_ε	Turbulent Prandtl number for epsilon
μ_t	Kinematic viscosity
C_μ	Coefficient for calculation of kinematic viscosity
$C_{1\varepsilon}$, $C_{2\varepsilon}$	Constants for kinetic energy and dissipation rate relations
h	Distance from the ground
u_r	Stream velocity at distance r
h_r	Reference distance from ground
A	Heliostat area
U	Stream velocity
C_{F_x}	Coefficient of drag force
F_x	Drag force acting on heliostat in x-axis direction
C_{F_z}	Coefficient of lift force
F_z	Lift force acting on heliostat in z-axis direction
Z_m	Height of the heliostat (m)
Z_h	Height of heliostat pedestal (m)
C_{Mh_y}	Coefficient of moment for calculation at heliostat hinge
C_{M_z}	Coefficient of moment for moment about z-axis
C_{M_y}	Coefficient of moment about y-axis (tumbling moment)
M_{h_y}	Moment about heliostat hinge
M_z	Moment about z-axis
M_y	Moment about y-axis

References

Abd Halim, M. A., Nik Mohd, N. A. R., Mohd Nasir, M. N., & Dahalan, M. N. (2018). The Evaluation of k-ε and k-ω Turbulence Models in Modelling Flows and Performance of S-shaped Diffuser. *International Journal of Automotive and Mechanical Engineering*, 15(2), 5161-5177. https://doi.org/10.15282/ijame.15.2.2018.2.0399

Abunajeeb, I., Stein, G., & Rotschild, C. (2025). Heliostat accurate control method robust under shading and blocking. *Energy Reports,* 13, 4087-4094. https://doi.org/10.1016/j.egyr.2025.03.047

Ali, K., & Jifeng, S. (2024). Analysis and Study on the Interference Effect of Tower Heliostats Based on Computational Wind Engineering. *Applied Solar Energy*, 60(2), 267-280. https://doi.org/10.3103/S0003701X23601527

Bakhshipour, S., Emes, M. J., & Arjomandi, M. (2025). Experimental study of dynamic wind loads on heliostats. *Journal of Wind Engineering and Industrial Aerodynamics,* 261, 106092. https://doi.org/10.1016/j.jweia.2025.106092

Bakhshipour, S., Emes, M. J., Jafari, A., & Arjomandi, M. (2024). Heliostat wind loads: Effects of the aspect ratio and ground clearance ratio. *Solar Energy*, 269, 112332. https://doi.org/10.1016/j.solener.2024.112332

Bendjebbas, H., Abdellah-ElHadj, A., & Abbas, M. (2016). Full-scale, wind tunnel and CFD analysis methods of wind loads on heliostats: A review. *Renewable and Sustainable Energy Reviews*, 54, 452-472. https://doi.org/10.1016/j.rser.2015.10.031

Blume, K., Röger, M., & Pitz-Paal, R. (2023). Full-scale investigation of heliostat aerodynamics through wind and pressure measurements at a pentagonal heliostat. *Solar Energy,* 251, 337-349. https://doi.org/10.1016/j.solener.2022.12.016

Blume, K., Röger, M., & Pitz-Paal, R. (2023). Simplified analytical model to describe wind loads and wind-induced tracking deviations of heliostats. *Solar Energy,* 256, 96-109. https://doi.org/10.1016/j.solener.2023.03.055

Coventry, J., & Pye, J. (2014). Heliostat Cost Reduction – Where to Now? *Energy Procedia,* 49, 60-70. https://doi.org/10.1016/j.egypro.2014.03.007

Devabhaktuni, V., Alam, M., Shekara Sreenadh Reddy Depuru, S., Green, R. C., Nims, D., & Near, C. (2013). Solar energy: Trends and enabling technologies. *Renewable and Sustainable Energy Reviews,* 19, 555-564. https://doi.org/10.1016/j.rser.2012.11.024

Dorian, J. P., Franssen, H. T., & Simbeck, D. R. (2006). Global challenges in energy. *Energy Policy*, 34(15), 1984-1991. https://doi.org/10.1016/j.enpol.2005.03.010

Emes, M. J., Arjomandi, M., & Nathan, G. J. (2015). Effect of heliostat design wind speed on the levelised cost of electricity from concentrating solar thermal power tower plants. *Solar Energy*, 115, 441-451. https://doi.org/10.1016/j.solener.2015.02.047

Emes, M. J., Jafari, A., Coventry, J., & Arjomandi, M. (2020). The influence of atmospheric boundary layer turbulence on the design wind loads and cost of heliostats. *Solar Energy*, 207, 796-812. https://doi.org/10.1016/j.solener.2020.07.022

Emes, M. J., Marano, M., & Arjomandi, M. (2024). Heliostat wind loads in the atmospheric boundary layer (ABL): Reconciling field measurements with wind tunnel experiments. *Solar Energy*, 277, 112742. https://doi.org/10.1016/j.solener.2024.112742

Emes, M., Jafari, A., Pfahl, A., Coventry, J., & Arjomandi, M. (2021). A review of static and dynamic heliostat wind loads. *Solar Energy,* 225, 60-82. https://doi.org/10.1016/j.solener.2021.07.014

Emes, M., Yellapantula, S., Sment, J., Armijo, K., Muller, M., Mehos, M., ... & Arjomandi, M. (2024). Heliostat Consortium: Gap Analysis on State of the Art in Wind Load Design. *Journal of Solar Energy Engineering*, 146(6), 061001. https://doi.org/10.1115/1.4065429

Fadlallah, S. O., Anderson, T. N., & Nates, R. J. (2021). Flow behaviour and aerodynamic loading on a stand-alone heliostat: Wind incidence effect. *Arabian Journal for Science and Engineering*, 46, 7303-7321. https://doi.org/10.1007/s13369-021-05405-0

Forman, P., Schellen, M., Schlichting, T., Pfahl, A., Mark, P., Glock, C., & Schnell, J. (2025). Design, construction, and qualification of a lightweight, modular heliostat made from high-performance concrete. *Solar Energy*, 285, 113093. https://doi.org/10.1016/j.solener.2024.113093

Fuqiang, W., Ziming, C., Jianyu, T., Yuan, Y., Yong, S., & Linhua, L. (2017). Progress in concentrated solar power technology with parabolic trough collector system: A comprehensive review. *Renewable and Sustainable Energy Reviews*, 79, 1314-1328. https://doi.org/10.1016/j.rser.2017.05.174

Grigoriev, V., Milidonis, K., Corsi, C., & Blanco, M. (2022). Heliostat fields with a balanced mirror density. Solar Energy, 243, 336-347. https://doi.org/10.1016/j.solener.2022.07.050

Hamidi, M. S. (2024). Direct numerical simulations of flow in dense fluid-particle systems (Doctoral dissertation, Université de Perpignan).

Hinkley, J. T., Hayward, J. A., Curtin, B., Wonhas, A., Boyd, R., Grima, C., Tadros, A., Hall, R., & Naicker, K. (2013). An analysis of the costs and opportunities for concentrating solar power in Australia. *Renewable Energy,* 57, 653-661. https://doi.org/10.1016/j.renene.2013.02.020

Jafari, A. (2020). Effects of Turbulence on Heliostat Wind Loads (Doctoral dissertation). https://hdl.handle.net/2440/135328

Ji, B., Qiu, P., Xu, F., Liu, Q., Zhang, X., & Zhang, L. (2023). Concentrating efficiency loss of heliostat with multiple sub-mirrors under wind loads. *Energy,* 281, 128281. https://doi.org/10.1016/j.energy.2023.128281

Jones, S., Lumia, R., Davenport, R., Thomas, R., Gorman, D., Kolb, G., & Donnelly, M. (2007). Heliostat Cost Reduction Study. Sandia Natl Lab. https://doi.org/10.2172/912923

Kandpal, T. C., & Broman, L. (2014). Renewable energy education: A global status review. *Renewable and Sustainable Energy Reviews,* 34, 300-324. https://doi.org/10.1016/j.rser.2014.02.039

Kjärstad, J., & Johnsson, F. (2009). Resources and future supply of oil. *Energy Policy,* 37(2), 441-464. https://doi.org/10.1016/j.enpol.2008.09.056

Li, W., Yang, F., Niu, H., Patruno, L., & Hua, X. (2024). Wind loads on heliostat tracker: A LES study on the role of geometrical details and the characteristics of near-ground turbulence. *Solar Energy*, 284, 113041. https://doi.org/10.1016/j.solener.2024.113041

Mahfoud, O., Moummi, A., Kadja, M., Noureddine, M., & Mebrouk, R. (2013). Dynamic and thermal study of air flow control by chicanes with inclined upper parts in solar air collectors. *International Journal of Sustainable Energy,* 34. https://doi.org/10.1080/14786451.2013.821125

Mahfoud, O., Danane, F., Debbache, M., Karoua, H., Takilalte, A., & Bouaichaoui, S. (2022, July). Wind action effects on heliostat–CFD and FEM study. *IOP Conference Series: Earth and Environmental Science, 1048(1), 012007.* IOP Publishing. https://doi:10.1088/1755-1315/1048/1/012007

Marano, M., Emes, M. J., Jafari, A., & Arjomandi, M. (2024). Effect of facet gap on heliostat wind loading. *Solar Energy*, 271, 112428. https://doi.org/10.1016/j.solener.2024.112428

Martín, P., Elena, V. B., Loredo-Souza, A. M., & Camaño, E. B. (2016). Experimental study of the effects of dish antennas on the wind loading of telecommunication towers. *Journal of Wind Engineering* *and Industrial Aerodynamics*, 149, 40-47. https://doi.org/10.1016/j.jweia.2015.11.010

Merarda, H., Aksas, M., & Andrianne, T. (2020). Shape effects on aerodynamic loading of heliostats. *Mechanics & Industry*, 21(6), 614. https://doi.org/10.1051/meca/2020086

Merarda, H., Toumi, M., & Boutelhig, A. (2024). Analysis of heliostat fatigue: Impact of wind speed distribution, studied over six regions of Algeria. *Solar Energy*, 278, 112776. https://doi.org/10.1016/j.solener.2024.112776

Mughal, K. H., Bugvi, S. A., Jamil, M. F., Baig, B. T., Ahmad, T., Irfan, M., ... & Gondal, A. A. (2022). Enhancement of Aerodynamic Performance of High Speed Train Through Nose Profile Design: A Computational Fluid Dynamics Approach. *Jurnal Kejuruteraan*, 34(6), 1237-1250. http://journalarticle.ukm.my/21128/

Natraj, Rao, B. N., & Reddy, K. S. (2021). Wind load and structural analysis for standalone solar parabolic trough collector. *Renewable Energy*, 173, 688-703. https://doi.org/10.1016/j.renene.2021.04.007

Pavlović, T. M., Radonjić, I. S., Milosavljević, D. D., & Pantić, L. S. (2012). A review of concentrating solar power plants in the world and their potential use in Serbia. *Renewable and Sustainable Energy Reviews,* 16(6), 3891-3902. https://doi.org/10.1016/j.rser.2012.03.042

Peterka, J. A., & Derickson, R. G. (1992). Wind load design methods for ground-based heliostats and parabolic dish collectors. https://www.osti.gov/servlets/purl/7105290

Peterka, J., Tan, Z., Cermak, J., & Bienkiewicz, B. (1989). Mean and peak wind loads on heliostats. *J. Sol. Energy Eng.* 111(2), 158-164. https://doi.org/10.1115/1.3268302

Pfahl, A., Buselmeier, M., & Zaschke, M. (2011). Wind loads on heliostats and photovoltaic trackers of various aspect ratios. *Solar Energy*, 85(9), 2185-2201. https://doi.org/10.1016/j.solener.2011.06.006

Shademan, M., Barron, R., Balachandar, R., & Hangan, H. (2014). Numerical simulation of wind loading on ground-mounted solar panels at different flow configuration. *Canadian Journal of Civil Engineering*. https://doi.org/10.1139/cjce-2013-0537

Sosa-Flores, P., Hinojosa, J. F., & Duran, R. L. (2022). Computational fluid dynamics study of the rear geometry influence on aerodynamic load coefficients of heliostats in stow position. *Solar Energy,* 241, 130-156. https://doi.org/10.1016/j.solener.2022.06.004

Sun, H., Gong, B., & Yao, Q. (2014). A review of wind loads on heliostats and trough collectors. *Renewable and Sustainable Energy Reviews,* 32, 206-221. https://doi.org/10.1016/j.rser.2014.01.032

TR, A., Kalpathy, S. K., & Thomas, T. (2025). Design and Assessment of a Linear Drive-Controlled Tilt-Roll Heliostat with Sun Tracking Algorithm for Small-Scale Solar Installation. *Energy Technology,* 13(3), 2401051. https://doi.org/10.1002/ente.202401051

Waqas, M., & Ahmad, N. (2020). Computation of Stress Distribution in Hydraulic Horizontal Propeller Turbine Runner Based on Fluid–Structure Interaction Analysis. *Arabian Journal for Science and Engineering*, 45(11), 9325-9337. https://doi.org/10.1007/s13369-020-04727-9

Yang, M., Zhang, Y., Wang, Q., Zhu, Y., & Taylor, R. A. (2022). A coupled structural-optical analysis of a novel umbrella heliostat. *Solar Energy,* 231, 880-888. https://doi.org/10.1016/j.solener.2021.12.018

Yu, J. S., Emes, M. J., Ghanadi, F., Arjomandi, M., & Kelso, R. (2019). Experimental investigation of peak wind loads on tandem operating heliostats within an atmospheric boundary layer. *Solar Energy,* 183, 248-259. https://doi.org/10.1016/j.solener.2019.03.002

Zang, C., Gong, B., & Wang, Z. (2014). Experimental and theoretical study of wind loads and mechanical performance analysis of heliostats. *Solar Energy*, 105, 48–57. https://doi.org/10.1016/j.solener.2014.04.003